Power Swing in Systems with Varying Penetration of Grid-forming IBRs: Protection and Dynamics

Xinquan Chen, *Graduate Student Member*, *IEEE*, Aboutaleb Haddadi, *Senior Member*, *IEEE*,
Evangelos Farantatos, *Senior Member*, *IEEE*, Ilhan Kocar, *Senior Member*, *IEEE*, and
Siqi Bu, *Senior Member*, *IEEE*

***Abstract*—Integration of inverter-based resources (IBRs) reshapes conventional power swing patterns, challenging the operation of legacy power swing protection schemes. This paper highlights the significant consequences of the distinctive power swing patterns exhibited by grid-forming IBRs (GFM-IBRs). The swing mechanism involving GFM-IBRs is elucidated using analytical modeling of GFM-IBRs with various power synchronization loops (PSLs). With varying GFM-IBR penetration levels and different generator scenarios, the performance of power swing protection functions is examined, including power swing blocking (PSB) and out-of-step tripping (OST). Additionally, the IEEE PSRC D29 test system is employed to present power swing protection results in a large-scale power system integrated with synchronous generators (SGs) and IBRs. The results indicate that, GFM-IBRs with sufficient voltage support capability can provide positive impact on power swing dynamics, and power swing protection performance can be enhanced by emulating the inertia and droop mechanism of SGs and rapidly adjusting the active power output. However, with high penetration levels of GFM-IBRs, OST maloperation may occur in scenarios with inadequate voltage support capability.**

***Index Terms*—Grid-forming, inverter-based resources, out-of-step, power swing, and power synchronization loop.**

I. INTRODUCTION

The increased uptake of inverter-based resources (IBRs) along with the retirement of synchronous generators (SGs) reduces system inertia due to IBRs' inability to supply kinetic energy from rotating components in the way that SGs can through their spinning rotors [1]–[3]. Traditional IBRs, which inject active and reactive power into the grid with minimal grid support functions, are commonly referred to as grid-following IBRs (GFL-IBRs). These IBRs exhibit power angle characteristics that differ from those of SGs, which may adversely affect the performance of protection schemes originally designed with the expectation of high inertia provided by SGs [4]–[6].

Enhanced IBRs that deliver full and fast frequency and voltage response are referred to as grid-forming IBR (GFM-IBR). These IBRs enhances system inertia through various primary control strategies, including virtual synchronous machine (VSM) control, droop control, and dispatchable virtual oscillator control (dVOC) [7], [8]. Depending on the primary control, a GFM-IBR can emulate the swing behavior of SGs through power-synchronization loops (PSLs) [9]. The inertial response of a GFM-IBR is determined by the employed control strategy and parameters [10], which in turn impacts the operation of system protection. Therefore, it is necessary to study the impact of GFM-IBR control settings on system dynamics and legacy protection schemes to ensure reliable protection as the proliferation of GFM-IBR increases [11]. The ultimate objective is to ensure that system protection remains reliable as power systems transition towards future IBR-dominated systems.

Power swing protection differentiates between a grid fault and a power swing condition and blocks the operation of designated distance zones upon detection of a power swing [12]–[15]. Increased uptake of GFL-IBRs reduces system inertia, leading to faster power swings that may not be detected by the Power Swing Blocking (PSB) function, thereby causing PSB maloperation. In addition, GFL-IBRs also change the swing impedance trajectory which may result in out-of-step-tripping (OST) malfunction and unwanted system partitioning during a stable power swing. Furthermore, as the penetration level of GFL-IBRs increases, the electrical center of the power system may shift, altering the optimal location for implementing OST protection [16]–[18].

Received: August 28, 2024
Accepted: December 16, 2024

Xinquan Chen and Siqi Bu are with the Department of Electrical and Electronic Engineering, The Hong Kong Polytechnic University, Hong Kong 999077, China (e-mail: xinquan.chen@connect.polyu.hk; siqi.bu@polyu.edu.hk).

Aboutaleb Haddadi and Evangelos Farantatos are with the Electric Power Research Institute (EPRI), Palo Alto 94301, USA (e-mail: ahaddadi@epri.com; efarantatos@epri.com).

Ilhan Kocar (corresponding author) is with Polytechnique Montreal, Montreal H3T 1J4, Canada (e-mail: ilhan.kocar@polymtl.ca).

DOI: 10.23919/PCMP.2024.000355

Existing research has identified that GFM-IBRs exhibit short-circuit fault characteristics [19] and power-angle behavior [20], distinct from those of SGs and GFL-IBRs. However, the impacts of GFM-IBRs on PSB and OST functions remain largely unexplored. Reference [21] presents the preliminary assessment of the virtual impedance-based GFM control during a power swing, indicating that a high virtual impedance can mitigate power flow oscillations by limiting fault current and underscoring the necessity for a more comprehensive investigation into the dynamics of power swings. References [22] and [23] propose a methodology for analyzing power swings in a system with IBRs, including dynamic modeling and commercial relay tests. This study highlights that the regulation of active power in GFM-IBRs is facilitated by PSLs that can emulate the swing dynamics of SGs, thereby making the power swing behavior of GFM-IBRs align with that of traditional SGs. However, there are no analytical elaborations or further studies on the impacts of GFM-IBRs on power swing protection. Reference [24] presents a comprehensive analysis of the rate of change (ROC) of the measured impedance trajectory during the re-synchronization process by analyzing the transient dynamic of the PSL, identifying the impacts of critical clearing angle and droop gain on power swing protection under re-synchronization conditions. However, this study focuses more on the transient stability perspective than on the protection perspective, and the relations between control settings and dynamics of power swing in the system with GFM-IBRs are not elaborated. Moreover, the power swing patterns with the high penetration level of GFM-IBRs have not been comprehensively investigated, leaving a gap in the current understanding of their behavior in power systems.

To bridge the above knowledge gaps, this paper contributes to providing innovative insights into power swing patterns in a system integrated with GFM-IBRs. Main contributions are listed as follows:

1) Power swing mechanism under the integration of GFM-IBR. Combining analytical modeling and the IEEE PSRC system simulation results, the relations between swing impedance and GFM control are elaborated, and the impacts of PSL parameters on swing impedance are explained.

2) Advantages and limitations of GFM-IBR during power swings. In the IEEE PSRC D6 and D29 systems, the power swing dynamics and the performance of PSB and OST are analyzed to evaluate the operation issues of power systems with varying GFM-IBR penetration levels during power swings.

3) Improvements. For GFM-IBR control solutions and protection settings during power swings to address the maloperation issues and enhance the system dynamics, considering energy storage devices.

II. INTERACTION BETWEEN GFM-IBR AND POWER SWING DYNAMICS

A. Relations between Swing Impedance and GFM Control

To study the relations between GFM-IBR and power swing dynamics analytically, a two-end transmission system integrated with a GFM-IBR is shown in Fig. 1. Z_{GFM}, Z_{tr}, and Z_{L} denote the equivalent impedances of GFM-IBR, IBR transformer, and transmission line, respectively, while $Z_{\mathrm{GFM}} = Z_{\mathrm{control}} + Z_{\mathrm{Filt}}$. Z_{control} and Z_{Filt} denote the respective controller impedance and equivalent filter impedance [25]. $\boldsymbol{V}_{\mathrm{GFM}}$ and $\boldsymbol{V}_{\mathrm{g}}$ denote the internal voltage vector of GFM-IBR and the grid voltage vector, respectively.

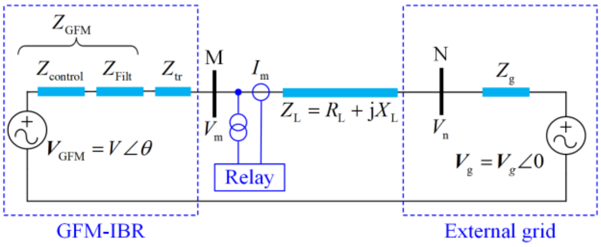

Fig. 1. Transmission system with GFM-IBRs for power swing illustration.

Figure 2 illustrates the closed-loop structure for generating internal voltage vectors of GFM-IBR, where the magnitude and phase of the internal voltage vectors are regulated by reactive power droop (Q-droop) control and PSL, respectively. The considered primary control modes, namely, droop, VSM and dVOC control, provide a generic representation of a number of GFM controls used in the power grid today.

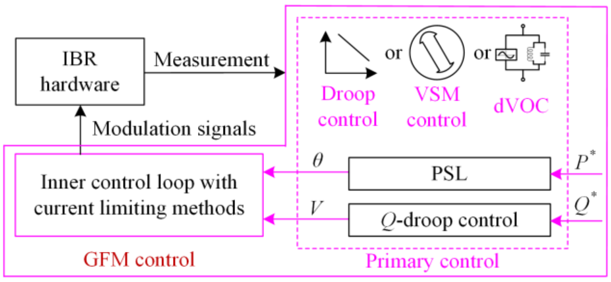

Fig. 2. Diagram of closed-loop structure for the generation of internal voltage vectors of GFM-IBR.

From Fig. 1, the apparent impedance measured by the distance relay during a power swing, i.e., swing impedance Z_{m}, is determined as:

$$Z_{\mathrm{m}} = \frac{V_{\mathrm{m}}}{I_{\mathrm{m}}} = \frac{\boldsymbol{V}_{\mathrm{GFM}} - (Z_{\mathrm{GFM}} + Z_{\mathrm{tr}})I_{\mathrm{m}}}{(\boldsymbol{V}_{\mathrm{GFM}} - \boldsymbol{V}_{\mathrm{g}})/(Z_{\mathrm{GFM}} + Z_{\mathrm{tr}} + Z_{\mathrm{L}})} = \frac{\boldsymbol{V}_{\mathrm{GFM}}(Z_{\mathrm{GFM}} + Z_{\mathrm{tr}} + Z_{\mathrm{L}})}{\boldsymbol{V}_{\mathrm{GFM}} - \boldsymbol{V}_{\mathrm{g}}} - (Z_{\mathrm{GFM}} + Z_{\mathrm{tr}}) \tag{1}$$

The phase difference between $\boldsymbol{V}_{\text{GFM}}$ and $\boldsymbol{V}_{\text{g}}$ is represented by the power angle δ. For simplicity, the phase of the grid voltage vector is set to zero in Fig. 1. Hence, the orientation angle equals the power angle, i.e., $\theta = \delta$. Considering $V_{\text{GFM}} \approx V_{\text{g}}$, (1) can be rewritten as:

$$Z_{\text{m}} \approx \frac{\boldsymbol{V}_{\text{g}}\angle\delta}{\boldsymbol{V}_{\text{g}}\angle\delta - \boldsymbol{V}_{\text{g}}\angle 0}(Z_{\text{GFM}}+Z_{\text{tr}}+Z_{\text{L}}) - (Z_{\text{GFM}}+Z_{\text{tr}}) = \left(\frac{Z_{\text{GFM}}+Z_{\text{tr}}+Z_{\text{L}}}{2}\right)\left(1-\text{j}\cot\frac{\delta}{2}\right) - (Z_{\text{GFM}}+Z_{\text{tr}}) \tag{2}$$

The detailed derivation process can be found in (A1) of the Appendix. From (2), the swing impedance trajectory can be altered by two impacting factors, i.e., power angle and equivalent output impedance of GFM-IBRs, which are determined by the PSL and controller impedance, respectively. For clarity, this study focuses on the impacts of various PSLs on swing impedance trajectory. PSLs in the VSM control, droop control, and dVOC are given by [26]:

$$\begin{cases} \omega_{\text{VSM}} = \dfrac{D_{\omega}(\omega^* - \omega) + (P^* - P)}{Js} \\ \omega_{\text{droop}} = \omega^* + D_{\text{P}} G_{\text{LPF,P}}(s)(P^* - P) \\ \omega_{\text{dVOC}} = \omega^* + \dfrac{\omega^* \kappa_1 G_{\text{LPF,P}}(s)}{(V^{\text{d}*})^2}(P^* - P) \end{cases} \tag{3}$$

where the low-pass filter $G_{\text{LPF,P}}(s) = \omega_{\text{P}}/(\omega_{\text{P}} + s)$; and ω_{P} denotes the cut-off frequency; J and κ_1 denote the virtual inertia and synchronization control gain, respectively; D_{ω} and D_{P} denote the damping coefficients for the frequency and active power, respectively.

From (3), tuning of these parameters can change the dynamics of angular frequency, even resulting in loss-of-synchronism (LOS), as illustrated in [27]. Since the line reactance is larger than the line resistance $(X_{\text{L}} \gg R_{\text{L}})$, the active power is approximately by:

$$P \approx V_{\text{m}} V_{\text{n}} \sin\delta / X_{\text{L}} \approx V_{\text{m}} V_{\text{n}} \delta / X_{\text{L}} \tag{4}$$

Combining (3) and (4) yields:

$$\begin{cases} \delta_{\text{VSM}} = \dfrac{P^*}{Js^2 + D_{\omega}s + V_{\text{m}}V_{\text{n}}/X_{\text{L}}} \\ \delta_{\text{droop}} = \dfrac{D_{\text{P}}\omega_{\text{P}}P^*}{s^2 + \omega_{\text{P}}s + D_{\text{P}}\omega_{\text{P}}V_{\text{m}}V_{\text{n}}/X_{\text{L}}} \\ \delta_{\text{dVOC}} = \dfrac{\omega^*\omega_{\text{P}}\kappa_1 P^*/(V^{\text{d}*})^2}{s^2 + \omega_{\text{P}}s + \omega^*\omega_{\text{P}}\kappa_1 V_{\text{m}}V_{\text{n}}\Big/\left(X_{\text{L}}(V^{\text{d}*})^2\right)} \end{cases} \tag{5}$$

From (5), the responses of power angle can be expressed by the standard 2nd-order transfer functions [27]. Based on this, the damping ratio ξ under various PSLs is derived as:

$$\begin{cases} \xi_{\text{VSM}} = \dfrac{D_{\omega}}{2\sqrt{J V_{\text{m}} V_{\text{n}} / X_{\text{L}}}} \\ \xi_{\text{droop}} = \dfrac{1}{2}\sqrt{\dfrac{\omega_{\text{P}} X_{\text{L}}}{V_{\text{m}} V_{\text{n}} D_{\text{P}}}} \\ \xi_{\text{dVOC}} = \dfrac{1}{2}\sqrt{\dfrac{(V^{\text{d}*})^2 \omega_{\text{P}} X_{\text{L}}}{V_{\text{m}} V_{\text{n}} \omega^* \kappa_1}} \end{cases} \tag{6}$$

From (2)−(6), under power swing conditions, the parameter tuning of PSLs can alter the damping ratios of power angle responses in a system with GFM-IBRs, thus affecting the power swing patterns as will be further analyzed through a case study.

B. Impacts of PSL Parameters on Swing Impedance

To analyze the impacts of PSL parameters on power swing patterns, a case study is conducted on the 500 kV IEEE PSRC D6 test system with generators G1−G4, as shown in Fig. A2. The details of the system and the approach to power swing generation can be found in [13] and [18], while G4 is replaced with GFM-IBR in this section. A stable power swing case is used to illustrate the power swing dynamics under different PSLs and varying parameters. The swing impedance trajectory is measured by R21.

Figure 3 illustrates that a decrease in virtual inertia J causes a higher damping ratio, leading to a shorter settling time and lower overshoot in δ. This validates the analysis in (6). When J is set to 1.5, δ shows significant oscillations, indicating a highly dynamic response, while P shows substantial oscillations, peaking around 1.5 p.u. and gradually stabilizing. When J is reduced to 0.15, δ exhibits moderate oscillations, stabilizing around 0.8 rad, while P shows smaller oscillations, stabilizing around 1 p.u. When J is further reduced to 0.015, δ remains relatively constant, suggesting minimal deviation from the initial state. Meanwhile, P initially exhibits rapid oscillations but stabilizes over time, indicating a transient response that settles. Hence, the smaller J also aggravates oscillations in transients. Figure 3(c) indicates that the swing impedance trajectory is related to the dynamic performance of δ, validating the analysis in (2). Overall, the results show that the PSL and its settings determine the dynamic performance of power angle. This alters the swing impedance trajectory and its ROC, potentially crossing protective elements and affecting the time delay for detection.

In addition, Figs. 4−6 exhibit that the larger D_{ω}, smaller D_{P}, and smaller κ_1 cause a higher damping ratio, respectively. For the responses of δ , the red line, blue line, and green line exhibit underdamping, critically damped, and overdamping conditions, respectively. Furthermore, the swing impedance trajectories are altered under varying dynamic performances of δ. These results follow the analysis in (2) and (6).

In (5), the transfer functions under droop control and dVOC are in the form of $aP^*/(s^2+\omega_p s+aV_m V_n/X_L)$, where a is a constant. Hence, the power swing dynamics under droop control and dVOC exhibit similarities, as shown in Figs. 5 and 6. Moreover, unlike the VSM control, there are significant oscillations when the damping ratio is low under droop control and dVOC. The reason lies in the additional virtual inertia loop in VSM control, whereas the droop control and dVOC only emulate the droop mechanism. To that end, the above results indicate that the control strategies and settings of GFM-IBR can alter the swing impedance trajectory and its ROC by the regulation of P and δ. The standard 2nd transfer functions illustrate how the PSL settings change the dynamic performance of δ by adjusting damping ratios.

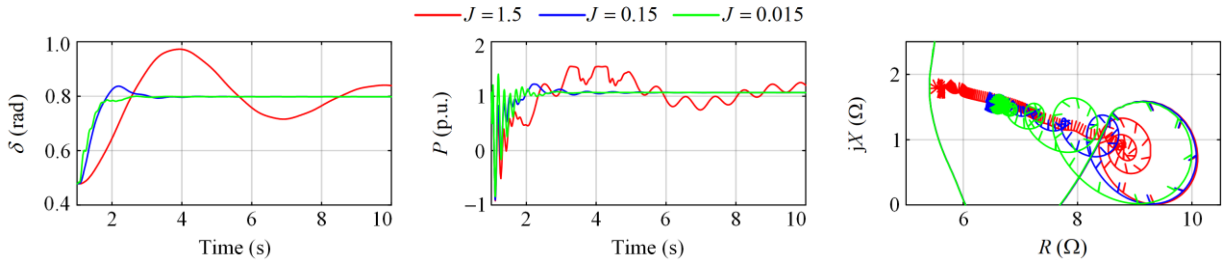

(a) (b) (c)

Fig. 3. Power swing dynamics with varying virtual inertia *J*. (a) Power angle. (b) Active power. (c) Apparent impedance.

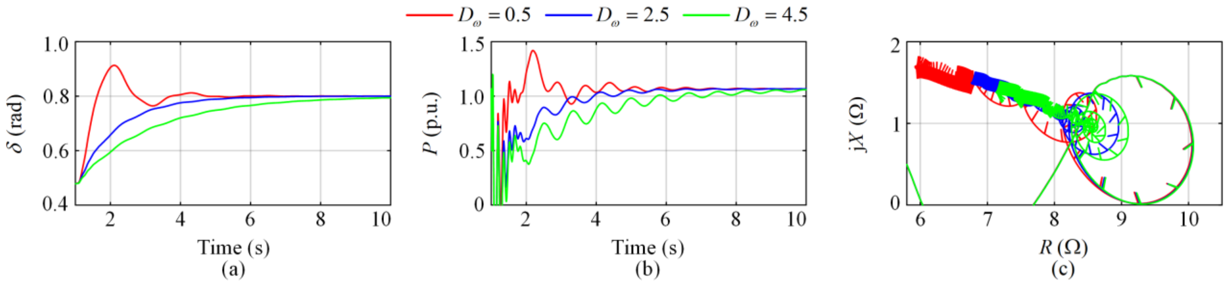

(a) (b) (c)

Fig. 4. Power swing dynamics with varying frequency damping coefficient D_ω. (a) Power angle. (b) Active power. (c) Apparent impedance.

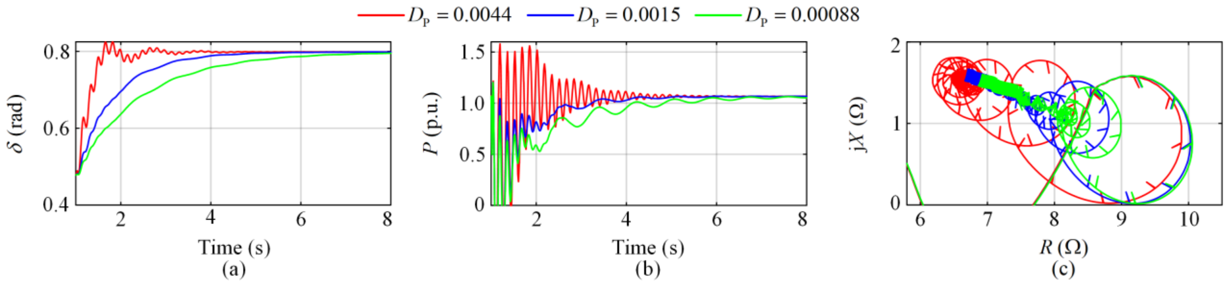

(a) (b) (c)

Fig. 5. Power swing dynamics with varying active power damping coefficient D_p. (a) Power angle. (b) Active power. (c) Apparent impedance.

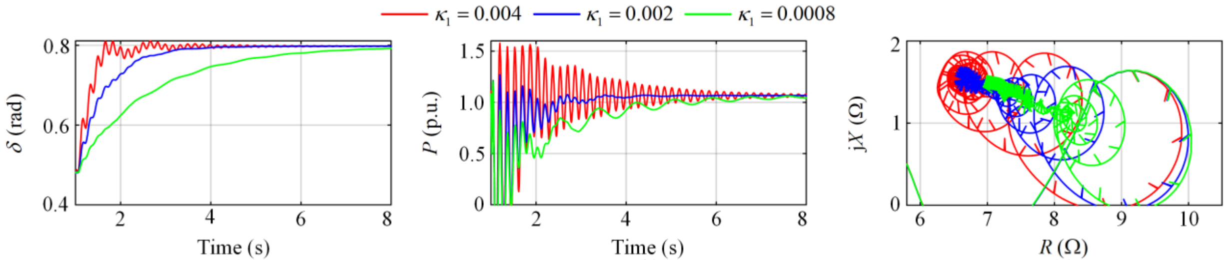

(a) (b) (c)

Fig. 6. Power swing dynamics with varying synchronization control gain κ_1. (a) Power angle. (b) Active power. (c) Apparent impedance.

III. IMPACTS OF GFM-IBR INTEGRATION ON POWER SWING PROTECTION

Section II has clarified how the GFM-IBR alters the swing impedance trajectory based on analytical modeling. However, in real-world scenarios, multiple IBRs are integrated into the power grid, resulting in more complex impacts on dynamic performance and protection systems. Therefore, from the protection perspective, the performance of power swing protection along with power swing dynamics are studied using the IEEE PSRC D6 test system under varying GFM-IBR penetration levels and different generator configurations, including GFM-IBR, SG, and GFL-IBR.

The PSB function measures the ROC of impedance using an outer and middle characteristics and a time delay setting of 3 cycles; if the trajectory crosses the outer and middle characteristics in more than 3 cycles, a power swing is detected, the PSB picks up and the distance relay zone is blocked, as shown in Fig. A1. However, if the trajectory crosses the two characteristics before 3 cycles, the event is classified as a non-swing, and the distance zones are not blocked. An unstable swing can be detected if: 1) the PSB function detects a power swing; and 2) the trajectory crosses the inner element. Based on this, an out-of-step signal is triggered when the time delay (one cycle in this paper) is exceeded or if the resistance exits the inner zone with a sign opposite to the one when entering the zone.

The detailed settings of R21 can be found in Table A1 of the Appendix. In this section, droop control is considered as the default control strategy of GFM-IBRs ($D_{\mathrm{P}}=1.2441$). Two typical power swing cases are utilized, as follows:

Case 1: The worst stable power swing under all SGs. The swing impedance trajectory almost reaches the inner blinders, which should be detected by the PSB function while the OST function should not trip.

Case 2: The fastest unstable power swing under all SGs. The ROC of the swing impedance trajectory is close to, but exceeds, 3 cycles under all SGs. The OST function should detect this.

A. Performance under Varying GFM-IBR Penetration Levels

For Case 1, Figs. 7 and 8 show the swing impedance trajectories and the responses of the PSB and OST functions of the relay in five scenarios, including 25% GFM-IBR (G1 is replaced with GFM-IBR), 50% GFM-IBR (G1 and G2 are replaced with GFM-IBRs), 75% GFM-IBR (G1−G3 are replaced with GFM-IBRs), and 100% GFM-IBR (G1−G4 are replaced with GFM-IBRs). Note that the percentage range (25%−100%) represents the capacity of GFM-IBRs as a proportion of the total capacity of generators G1−G4.

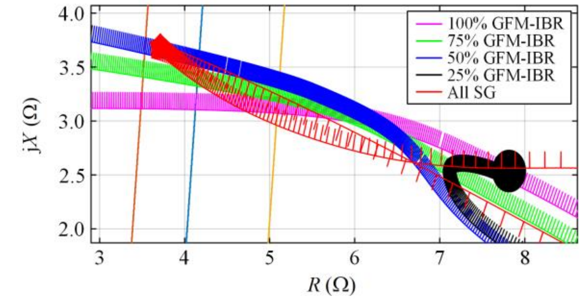

Fig. 7. Swing impedance trajectory under varying GFM-IBR penetration levels (Case 1).

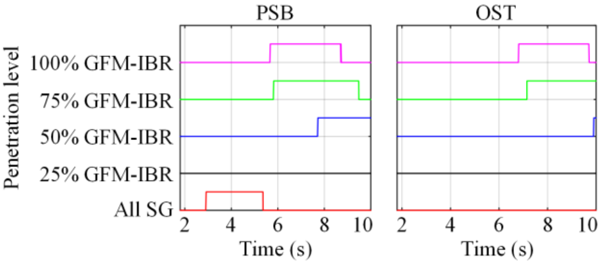

Fig. 8. Power swing relay signals under varying GFM-IBR penetration levels (Case 1).

The key results of the power swing protection of R21 are obtained, as listed in Table I, where Z_{outer}, Z_{middle}, and Z_{inner} denote the intersection points between a swing impedance trajectory and outer, middle, and inner elements, respectively. Correspondingly, t_{o}, t_{m}, and t_{i} denote respective timepoints.

TABLE I
POWER SWING PROTECTION RESULTS UNDER VARYING GFM-IBR INTEGRATION LEVELS (CASE 1)

Integration level	Outer element		Middle element		Inner element			Tripping results (1: Trip; 0: No Trip)
	Z_{outer} (Ω)	t_{o} (s)	Z_{middle} (Ω)	t_{m} (s)	Z_{inner} (Ω)	t_{i} (s)	>1 cycle?	
100% GFM-IBR	5.09+j3.07	**5.627**	4.13+j3.1	**6.354**	3.48+j3.11	**6.795**	Yes	PSB=1, OST=1 (Unstable and correct)
75% GFM-IBR	5.1+ j3.18	**5.774**	4.15+j3.32	**6.638**	3.51+j3.41	**7.134**	Yes	PSB=1, OST=1 (Unstable and correct)
50% GFM-IBR	5.11+j3.31	**7.675**	4.16+j3.5	**9.235**	3.53+j3.62	**9.891**	Yes	PSB=1, OST=1 (Unstable and correct)
25% GFM-IBR	-	-	-	-	-	-	-	**PSB=0, OST=0** **(Stable and correct)**
All SG	5.08+j2.96	**2.879**	4.15+j3.35	**3.347**	-	-	-	PSB=1, OST=0 (Stable and correct)

Under SG, during 2.879–3.347 s, the swing impedance trajectory crosses the outer and middle elements in more than 3 cycles, and the PSB function picks up as expected. The impedance trajectory reverses direction and exits the inner elements. Hence, the impedance trajectory does not cross the inner characteristic, and the OST function does not pick up as expected.

Under 25% GFM-IBR, the swing impedance trajectory does not enter the outer element and settles in an operating point corresponding to 7.83+j2.57 Ω. Hence, neither PSB nor OST picks up, which is the correct operation. The result suggests that integrating GFM-IBRs can enhance the efficiency of power system restoration and reduce the duration of power swing conditions.

Under 50%–100% GFM-IBR, the swing impedance trajectories cross the outer and middle elements in more than 5 cycles, and the PSB function successfully detects it. However, although these impedance trajectories move slowly, they ultimately cross and fall inside the inner characteristic. Since the time delay (one cycle) is exceeded, the OST function declares an out-of-step condition. In Table I, higher penetration of GFM-IBRs leads to smaller t_{o}, t_{m}, and t_{i}, improving the ROC of swing impedance, and shortening the activation time of the PSB and OST in Fig. 8.

For clear understanding, Fig. 9 compares the active power output and phase of SG, GFL-IBR, and GFM-IBR under the power swing event. Under all SG and 25% GFM-IBR, the P and δ can stabilize under the worst power swing conditions. This result indicates that the integration of GFM-IBR can quickly change its active power output and phase angle due to its emulation of swing behavior, exhibiting better dynamic performance and improving the power angle stability under power swing conditions.

Furthermore, Fig. 9(a) shows that 50%–100% GFM-IBRs cannot support sufficient active power output, leading to a diverging power angle in Fig. 9(b). Hence, GFM-IBRs lose synchronization with the power grid. Consequently, swing impedance trajectories cross the inner element, as shown in Fig. 7. Finally, both PSB and OST functions are activated in Fig. 8.

For Case 2, Figs. 10 and 11 along with Table II show the swing impedance trajectories, the responses of the PSB and OST functions, and key results of the power swing protection during an unstable power swing.

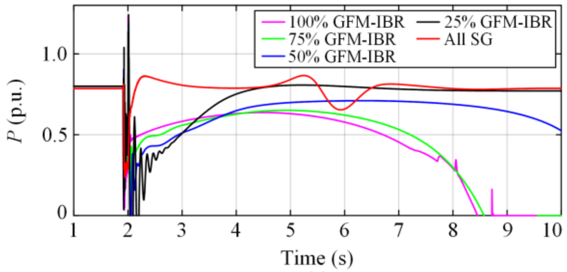

(a)

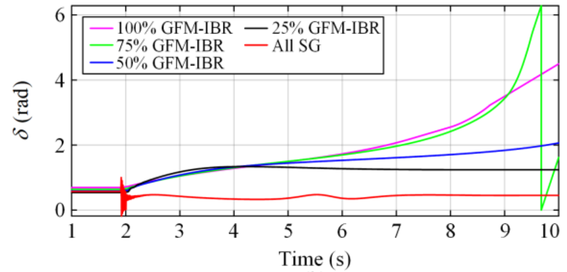

(b)

Fig. 9. Power swing dynamics under varying GFM-IBR penetration levels (Case 1). (a) Active power. (b) Power angle.

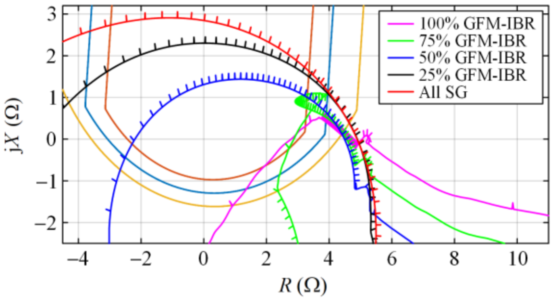

Fig. 10. Swing impedance trajectory under varying GFM-IBR penetration levels (Case 2).

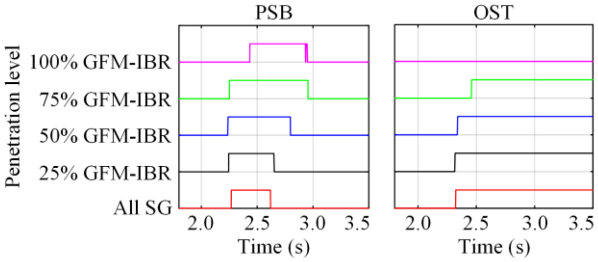

Fig. 11. Power swing relay signals under varying GFM-IBR penetration levels (Case 2).

Under SGs, the swing impedance trajectory crosses the outer and middle elements at 2.22 s and 2.274 s, respectively, corresponding to a time delay of 3.3 cycles. Since this time delay is larger than the PSB setting of 3 cycles, the PSB function successfully detects the power swing. Further, the OST function picks up when the swing impedance trajectory crosses the inner element at 2.315 s and the time delay (one cycle) is exceeded.

Under 25%–75% GFM-IBR, the swing impedance trajectory crosses the outer and middle elements at the respective t_{o} and t_{m}. Since the time delay is more than the PSB time delay setting, and hence, the PSB elements successfully detect the swing and issue a PSB signal, while the OST declares an unstable swing upon crossing the inner element at $(t_{\mathrm{i}}+1\ \text{cycle})$.

Under 100% GFM-IBR, the swing impedance trajectory crosses the outer and middle elements at 2.373 s and 2.916 s, respectively, corresponding to a time delay of 33.9 cycles, which is more than the PSB time delay setting. Consequently, the PSB detects the swing as expected. However, although the impedance trajectory crosses the inner element, the OST function fails to declare an unstable swing. This is because the impedance trajectory enters the inner element at 2.927 s and exits the inner element at 2.936 s, corresponding to a time delay of 0.5 cycles, which is less than the time delay. In addition, the resistance exits the inner zone with the same sign as it entered, which does not satisfy the OST function criteria.

TABLE II
POWER SWING PROTECTION RESULTS UNDER VARYING GFM-IBR INTEGRATION LEVELS (CASE 2)

Integration level	Outer element		Middle element		Inner element			Tripping results (1: Trip; 0: No Trip)
	Z_{outer} (Ω)	t_o (s)	Z_{middle} (Ω)	t_m (s)	Z_{inner} (Ω)	t_i (s)	>1 cycle?	
100% GFM-IBR	4.68+j0.43	2.373	3.93+j0.82	2.916	3.26+j0.49	2.927	**No**	**PSB=1, OST=0** **(Unstable and misoperation)**
75% GFM-IBR	4.7+j0.46	2.196	3.93+j0.88	2.334	3.3+j1.01	2.45	Yes	PSB=1, OST=1 (Unstable and correct)
50% GFM-IBR	4.67+j0.42	2.185	3.95+j1.03	2.271	3.33+j1.32	2.33	Yes	PSB=1, OST=1 (Unstable and correct)
25% GFM-IBR	4.64+j0.39	2.197	3.95+j1.1	2.262	3.34+j1.5	2.309	Yes	PSB=1, OST=1 (Unstable and correct)
All SG	4.64+j0.38	2.22	3.95+j1.15	2.274	3.35+j1.63	2.315	Yes	PSB=1, OST=1 (Unstable and correct)

The above results indicate that varying GFM-IBR penetration level alters the unstable swing impedance trajectory and its ROC. In Fig. 12(a), the dynamics of their active power output are significantly different although GFM-IBRs emulate the swing behavior of SGs. Under GFM controls, significant and rapid oscillations in active power output pose a challenge to transient stability. In Fig. 12(b), the power angle diverges, indicating the LOS of GFM-IBRs. Under 50%~100% GFM-IBRs, the voltage ride-through requirements cannot be met since the GFM-IBRs cannot provide sufficient spinning reserve. Consequently, the active power outputs decrease to zero after t=2.9 s due to the disconnection of GFM-IBRs from the power grid.

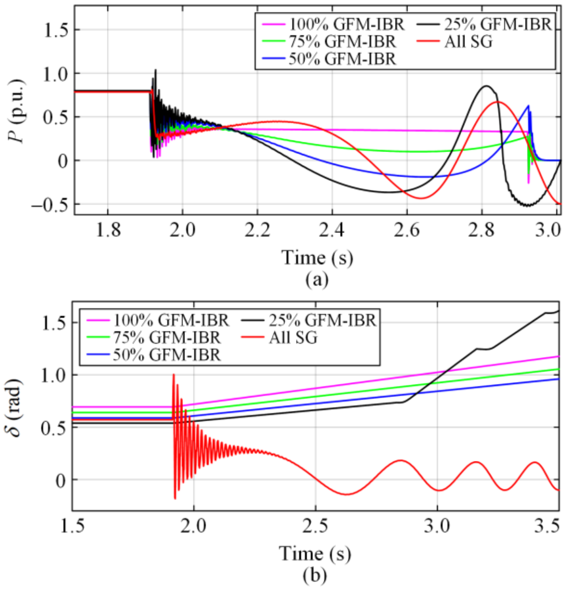

Fig. 12. Power swing dynamics under varying GFM-IBR penetration levels (Case 2). (a) Active power. (b) Power angle.

Fundamentally, the maloperation is caused by the insufficient voltage support capability of a system dominated by GFM-IBRs. Figure 13 shows the voltage ride-through curves under 75% and 100% GFM-IBR for illustration. The voltage ride-through function starts up at the inception of faults (t=1.91 s). Hydro Quebec requirements are used in this paper [28]. When t is 2.9 s, the voltage ride-through protection picks up, leading to the swing impedance crossing the inner element, as shown in Fig. 10.

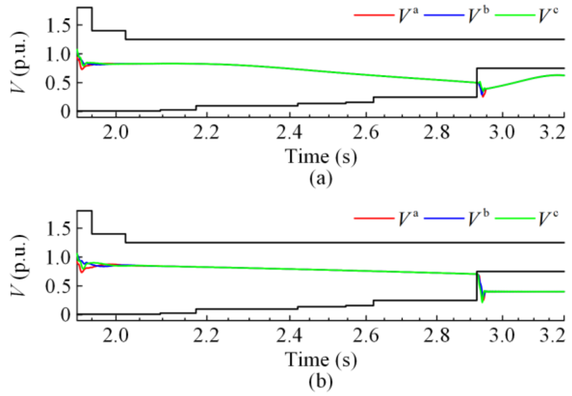

Fig. 13. Voltage ride-through curves under varying GFM-IBR penetration levels. (a) 75% GFM-IBR. (b) 100% GFM-IBR.

B. Comparison with SGs and GFL-IBRs

Figures 14 and 15 compare the swing impedance trajectories and responses of PSB and OST functions under all SGs, 25% GFL-IBR, and 25% GFM-IBR (VSM or droop control) for Case 1 with $D_p = 1.2441$, $J = 0.15$, and $D_\omega = 0.8038$. Under SGs, the swing trajectory reverses direction and settles at a new operating point corresponding to 9.77+j1.97 Ω. Hence, the PSB element flags a stable power swing. Under 25% GFM-IBR, the swing impedance trajectory does not enter the outer blinders and settles at an operating point corresponding to 7.83+j2.57 Ω. No swing is detected in this scenario either. In contrast, the swing impedance trajectory under 25% GFL-IBR crosses the outer, middle, and inner elements. The time delay exceeds the PSB and OST settings. Hence, the PSB and OST elements detect an unstable swing.

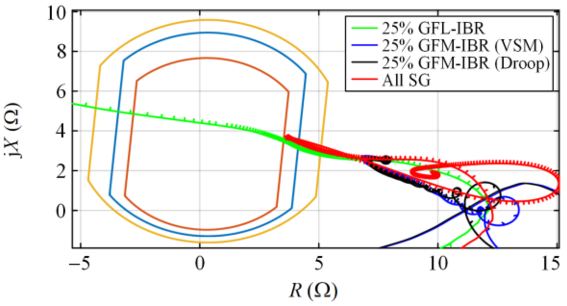

Fig. 14. Comparison of swing impedance trajectory under SG, GFL-IBR, and GFM-IBR (Case 1).

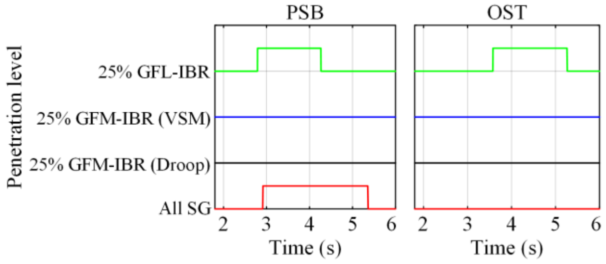

Fig. 15. Power swing relay signals under SG, GFL-IBR, and GFM-IBR (Case 1).

Figure 16 shows that P and δ cannot stabilize under 25% GFL-IBR, indicating that the GFL-IBR cannot retain synchronism under power swing conditions. Hence, both PSB and OST functions trip under 25% GFL-IBR. In contrast, the responses can converge quickly under SGs and GFM-IBRs, suggesting that GFM-IBR can mitigate the LOS issue typically caused by GFL-IBR. This is because GFM-IBR can quickly adjust its active power output back to the nominal value in response to a change in δ.

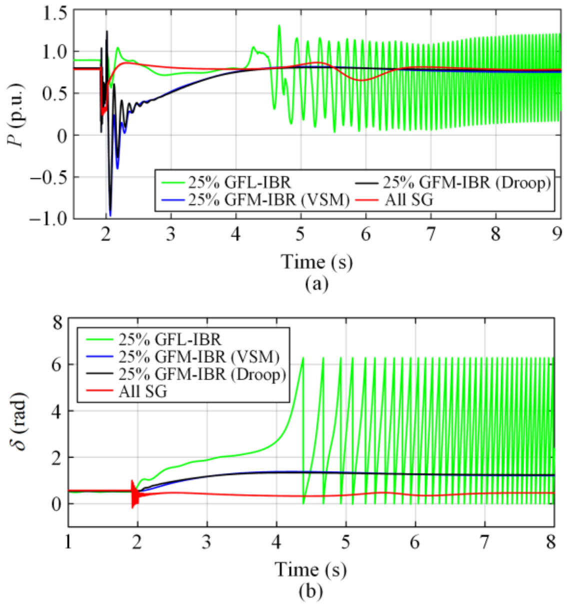

Fig. 16. Comparison of power swing dynamics under SG, GFL-IBR, and GFM-IBR (Case 1). (a) Active power. (b) Power angle.

For Case 2, Figs. 17 and 18 compare the unstable swing impedance trajectories and responses of PSB and OST functions under three different combinations of generators. The results under all SGs and 25% GFM-IBR have already been shown in Section III.A. Under 25% GFL-IBR, the swing crosses the outer and middle elements at $t_{\mathrm{o}} = 2.200$ s and $t_{\mathrm{m}} = 2.225$ s, respectively, corresponding to a time delay of 1.5 cycles, which is less than the PSB time delay setting. Consequently, the PSB function fails to detect the swing, and the OST function also fails to declare an unstable swing since the reduced inertia under GFL-IBR results in a higher ROC of swing impedance.

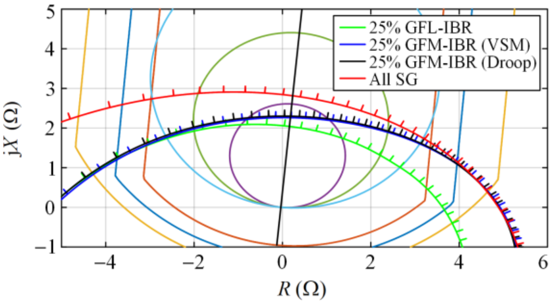

Fig. 17. Comparison of swing impedance trajectory under SG, GFL-IBR, and GFM-IBR (Case 2).

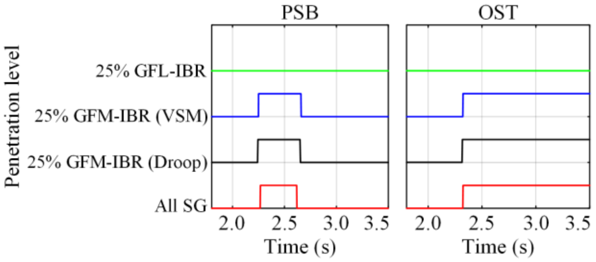

Fig. 18. Power swing relay signals under SG, GFL-IBR, and GFM-IBR (Case 2).

Moreover, with the integration of IBRs, the electrical centers are shifted, causing the impedance trajectories to cross into Zone 1 of the distance protection. Consequently, the Zone 1 signal is triggered, as illustrated in Fig. 19. With 25% GFM-IBR, the PSB function is activated, preventing the distance protection from tripping. However, with 25% GFL-IBR, the PSB function is not triggered, leading to the maloperation of the distance protection.

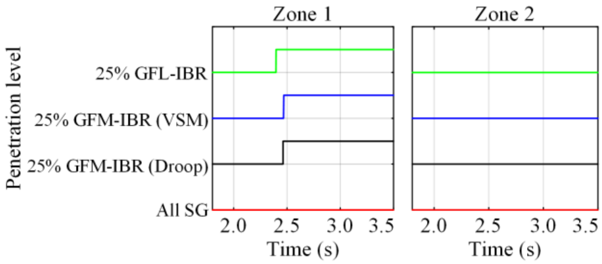

Fig. 19. Distance relay signals under SG, GFL-IBR, and GFM-IBR (Case 2).

Figure 20 compares δ under different generator scenarios, showing that GFM-IBR can enhance power angle stability, whereas GFL-IBR loses synchronization. Overall, the above comparison cases indicate that GFM-IBRs, when equipped with sufficient voltage support capability, can help prevent the potential maloperation of PSB and OST functions that typically caused by GFL-IBR.

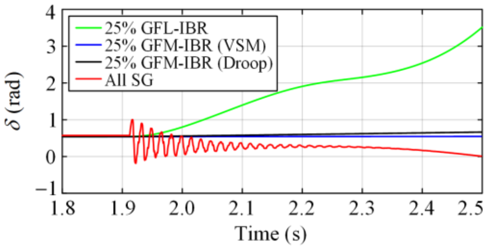

Fig. 20. Comparison of power angle under SG, GFL-IBR, and GFM-IBR (Case 2).

IV. POWER SWING IN LARGE-SCALE SYSTEM WITH IBR

A. IEEE PSRC D29 Test System

To further illustrate the impact of GFM-IBR on power swing protection in a large-scale power system, an additional case study is conducted on the IEEE PSRC D29 test system [18], as shown in Fig. A3. A unstable power swing is simulated by applying a midline fault on the line from Bus 12 to Bus 15, followed by the outage of the line through the opening of line terminal breakers. Power swing protection is implemented by a relay close to Bus 8. In this section, the VSM control is employed in GFM-IBRs. The generation scenarios are: All SG–All generators are synchronous generators; 41% IBR–G3, G4, G6, and G16, which constitute 41% of the installed capacity, are replaced by IBRs; 27% IBR–G16 is replaced by IBR; and 14% IBR–G3, G4, and G6 are replaced by IBRs.

B. Power Swing Performance

In the IEEE PSRC D29 test system, power swing patterns are examined for scenarios with all SG, 27% GFM-IBR, and 41% GFM-IBR, as demonstrated in Figs. 21 and 22, to explore the performance under low GFM-IBR penetration levels ($<50\%$). In the scenario with all SG, the swing impedance trajectory crosses the outer, middle, and inner elements, exceeding the PSB and OST time delay settings. Consequently, the PSB and OST signals are triggered at 2.59 s and 4.79 s, respectively. When the system includes 27% GFM-IBR and 41% GFM-IBR, the PSB activation time increases to 2.8 s and 4.19 s, respectively, indicating slower swing impedance trajectories. Moreover, these impedance trajectories do not enter the inner element, so the OST signals are not triggered, as expected.

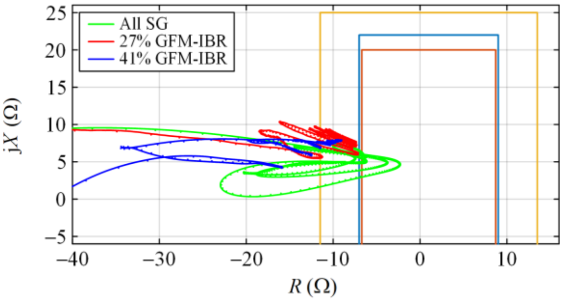

Fig. 21. Swing impedance trajectory for R21 under varying GFM-IBR penetration levels.

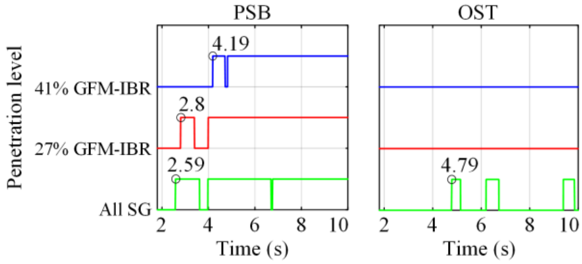

Fig. 22. Power swing relay signals of R21 under varying GFM-IBR penetration levels.

Furthermore, Figs. 23 and 24 compare the power swing patterns in a large-scale power system integrated with SGs, GFL-IBRs, and GFM-IBRs, including scenarios with all SG, 27% GFL-IBR+14% GFM-IBR, and 14% GFL-IBR+27% GFM-IBR. Under 27% GFL-IBR+14% GFM-IBR, the PSB and OST activation times reduce to 2.47 s and 4.3 s, respectively, due to the reduced inertia and faster ROC of swing impedance. Under 14% GFL-IBR+27% GFM-IBR, the PSB activation time increases to 2.65 s, indicating a slower power swing. The impedance trajectory does not enter the middle and inner elements, so the OST signal is not triggered. Overall, the above results further demonstrate the positive impact of GFM-IBR on power swing protection.

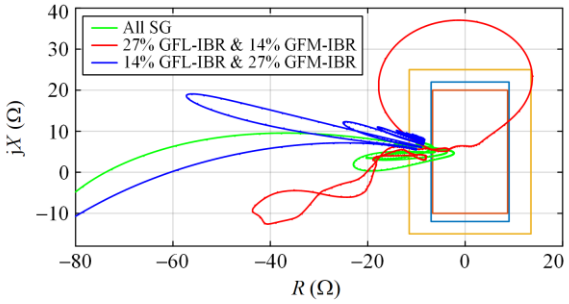

Fig. 23. Comparison of swing impedance trajectory for R21 under SG, GFL-IBR, and GFM-IBR.

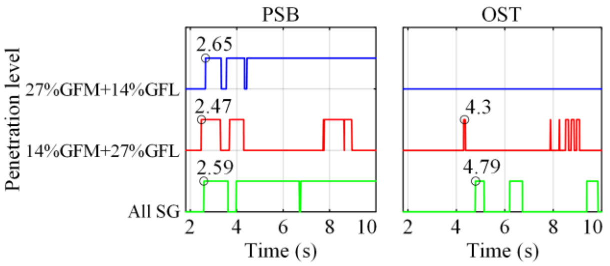

Fig. 24. Power swing relay signals of R21 under SG, GFL-IBR, and GFM-IBR.

V. IMPROVEMENTS FOR GFM-IBR DURING POWER SWING

Based on the above analysis, there are operational issues of GFM-IBRs during power swings. Considering state-of-the-art techniques, improvements are proposed as follows:

From the protection perspective, to avoid this OST maloperation issue, improvements include: 1) readjusting the time delay for the OST function; or 2) optimizing the allocation of the spinning reserve, e.g., the employment of battery energy storage system (BESS) [29]. For example, in the IEEE PSRC D6 test system (Case 2), a STATCOM with energy storage devices is applied at Bus A. Figures 25–27 compare the voltage ride-through curve, swing impedance trajectory, and relay signals. With energy storage devices, the OST function can correctly detect the swing.

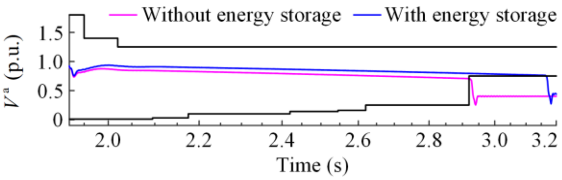

Fig. 25. Original and improved voltage ride-through curves when G1–G4 are replaced by GFM-IBRs (Case 2).

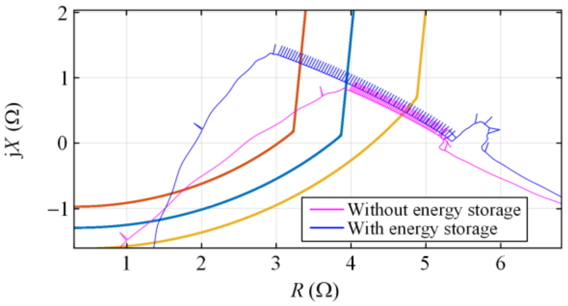

Fig. 26. Original and improved swing impedance trajectory when G1–G4 are replaced by GFM-IBRs (Case 2).

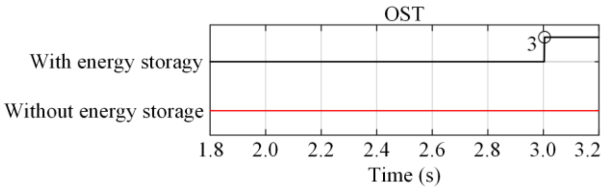

Fig. 27. Original and improved relay signals when G1–G4 are replaced by GFM-IBRs (Case 2).

From the dynamic perspective, the instability phenomenon in Case 1 under high-penetration GFM-IBR is caused by unstable inner voltage regulation. From Fig. 28, the *q*-axis current reference (output of inner voltage control) diverges, indicating that the inner voltage control cannot stabilize.

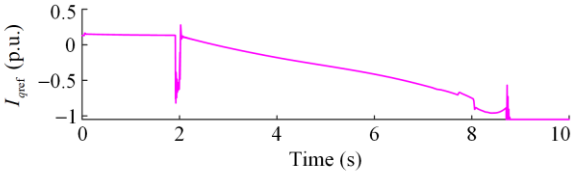

Fig. 28. q-axis current reference ($I_{q\mathrm{ref}}$) of G4 when G1–G4 are replaced by GFM-IBRs (Case 2).

The synchronizing and damping torque analysis indicate that the inner voltage control causes the negative damping torque components on the PSL [30]–[32], as illustrated by Fig. 29. K and D denote the synchronizing and damping torque coefficients, respectively.

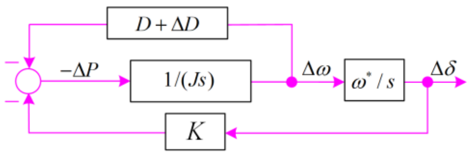

Fig. 29. Equivalent Phillips-Heffron modeling of GFM-IBR for synchronizing and damping torque analysis.

The additional damping torque component ΔD induced by the inner control is given by [31]:

$$\Delta D=\frac{-2\omega^{*}\omega^{2}V_{\mathrm{g}}^{2}K_{\mathrm{pV}}K_{\mathrm{iV}}L_{\Sigma}}{\left[L_{\Sigma}^{2}\left(K_{\mathrm{iV}}^{2}-K_{\mathrm{pV}}^{2}\omega^{2}\right)-\omega^{2}\right]^{2}+4\omega^{2}K_{\mathrm{pV}}^{2}K_{\mathrm{iV}}^{2}L_{\Sigma}^{4}} \tag{7}$$

where $\omega^{*}L_{\Sigma}=\mathrm{Im}\,(Z_{\mathrm{GFM}}+Z_{\mathrm{tr}}+Z_{\mathrm{L}})$; L_{Σ} denotes the equivalent inductance; while K_{pV} and K_{iV} denote the PI parameters of inner voltage control. Detailed model derivation can be found in [31].

Equation (7) explains how the inner voltage control parameters and equivalent impedance impact the damping torque. The system is stable when $K>0$ and $D+\Delta D>0$. To enhance system stability during power swings, improvements for GFM-IBR include tuning the inner voltage control parameters and adjusting the equivalent impedance.

Virtual impedance-based (VI-based) control is a potential solution to adjust the variable magnitude of Z_{GFM}, thereby enhancing the damping torque [32]. Details of the controller can be found in [33]. In the IEEE PSRC D6 test system when G1–G4 are replaced by GFM-IBRs (Case 1), Fig. 30 shows the power swing dynamics under the regulation of VI-based control, while Fig. 31 shows the magnitude of the variable virtual impedance (Z_{VI}). As seen, during the power swing, the incremental magnitude of the VI is around 0.145 p.u., thereby mitigating the negative torque through the impedance increment [32].

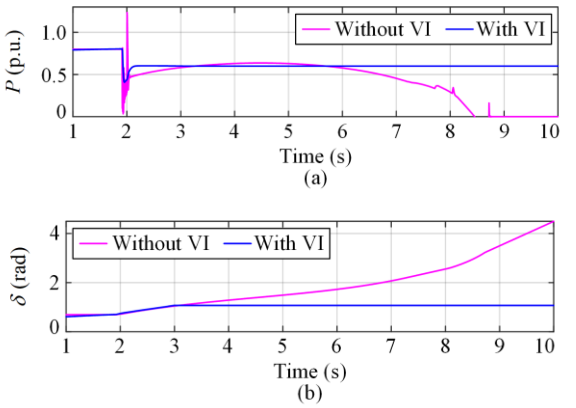

Fig. 30. Original and improved power swing dynamics when G1–G4 are replaced by GFM-IBRs (Case 1). (a) Active power. (b) Power angle.

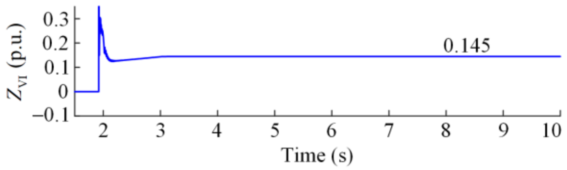

Fig. 31. Magnitude of the variable virtual impedance during power swing (Case 1).

VI. CONCLUSION

This paper investigates the impact of GFM-IBRs on power swing protection across varying penetration levels and generator scenarios. Key conclusions are drawn as follows:

1) Mechanism. The analytical modeling combines existing P-δ models and the derived swing impedance model to explain the relations among swing impedance and power swing patterns. Analysis and simulation results demonstrate how PSL settings influence the power swing dynamics by altering damping ratios, thereby modifying the swing impedance trajectory.

2) Advantages. GFM-IBRs can rapidly adjust their active power output and phase angle, enhancing dynamic performance and power angle stability under stable power swing conditions. With sufficient voltage support capability, GFM-IBRs can effectively mitigate the potential maloperation of PSB and OST functions typical caused by GFL-IBRs, thus positively enhancing the performance of power swing protection. The integration of GFM-IBRs improves the ROC of swing impedance, shortening the activation time of power swing functions.

3) Limitations. The frequency and voltage support capabilities of GFM-IBRs highly rely on the PSL and inner voltage control, which potentially may lead to insufficient damping torque and violate voltage ride-through requirements. OST maloperation occurs when G1–G4 are replaced by GFM-IBRs during unstable power swings due to: (a) the impedance trajectory enters and exits the inner element with the same sign of resistance; and (b) with a time delay of 0.5 cycles less than the time delay.

4) Improvements. From the protection perspective, to avoid OST maloperation, improvements include: ① readjusting the time delay for the OST function; or ② optimizing the allocation of the spinning reserve, e.g., the employment of BESS to enhance the damping of power swing. From the dynamic perspective, improvements for GFM-IBRs include inner voltage parameter tuning and controller impedance increment, e.g., the utilization of VI-based control to attenuate the negative torque components through impedance increments.

Future research efforts can focus on robust synchronization methods for improving power swing patterns with high penetration levels of GFM-IBRs and optimal allocation of additional reserve power.

APPENDIX A

This paper focuses on the protective relay that utilizes a mho-with-blinders detection scheme, which features three concentric circles constrained by three sets of blinders [18]. The settings of the PSB function are typically determined based on the fastest power swing, and the settings of the OST function are derived from the swing impedance trajectory of the most severe stable swing.

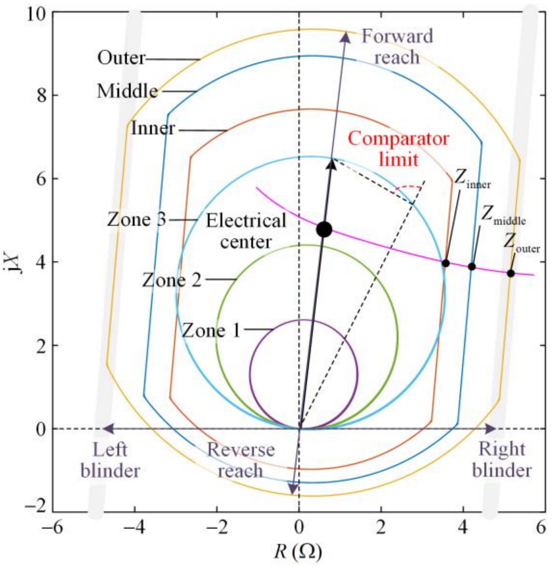

Fig. A1. Zones and blinders of the protective relay R21.

TABLE AI
SETTINGS OF PROTECTIVE RELAY R21

	Protection functions and settings	Value
PSB&OST	Shape	Mho with blinders
	Mode	3-step
	Trip mode	Instantaneous
	I1pkp/I2pkp (p.u.)	0.1/0.1
	Forward/reverse reach outer (Ω)	300/50
	Forward/reverse reach middle (Ω)	280/40
	Forward/reverse reach inner (Ω)	240/30
	PSB delay (s)	0.048
	Reset delay 1 (s)	0.16
	OST time delay (s)	0.017
	Delay seal in (s)	1

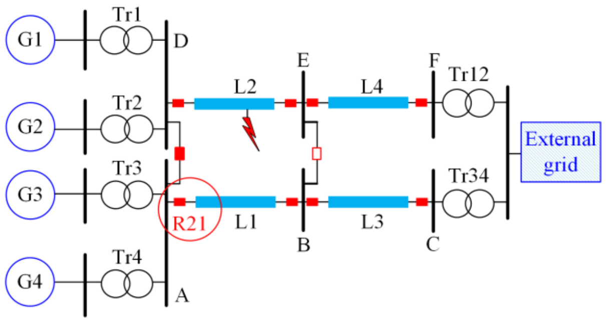

Fig. A2. IEEE PSRC D6 test system with GFM-IBR.

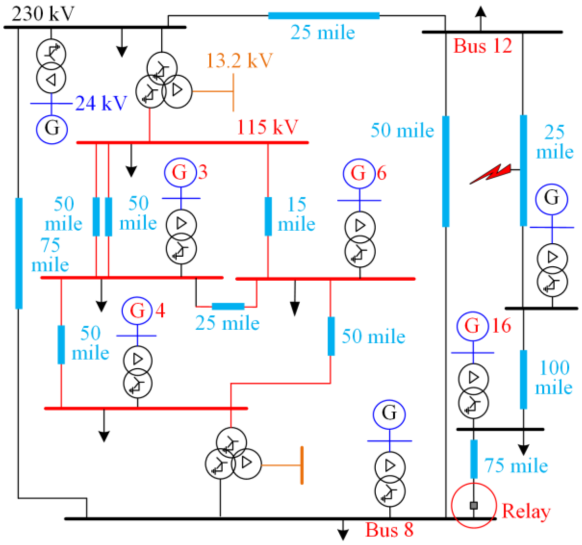

Fig. A3. IEEE PSRC D29 test system with GFM-IBR.

Detail derivation in (2):

$$\begin{aligned}
&\frac{V_g\angle\delta}{V_g\angle\delta - V_g\angle 0} = \frac{1}{1-1\angle-\delta} = \\
&\frac{1}{1-\cos\delta+\mathrm{j}\sin\delta} = \frac{1-\cos\delta-\mathrm{j}\sin\delta}{(1-\cos\delta)^2+(\sin\delta)^2} = \\
&\frac{1-\cos\delta-\mathrm{j}\sin\delta}{2-2\cos\delta} = \frac{1}{2}\left(1-\mathrm{j}\frac{\sin\delta}{1-\cos\delta}\right) = \\
&\frac{1}{2}\left[1-\mathrm{j}\frac{2\cos(\delta/2)\sin(\delta/2)}{1-\left(\cos(\delta/2)\right)^2+\left(\sin(\delta/2)\right)^2}\right] = \\
&\frac{1}{2}\left[1-\mathrm{j}\frac{2\cos(\delta/2)\sin(\delta/2)}{2\left(\sin(\delta/2)\right)^2}\right] = \frac{1}{2}\left(1-\mathrm{j}\cot\frac{\delta}{2}\right)
\end{aligned} \tag{A1}$$

ACKNOWLEDGMENT

Not applicable.

AUTHORS' CONTRIBUTIONS

Xinquan Chen: conceptualization, investigation, methodology, software, validation, and writing. Aboutaleb Haddadi: project administration, supervision, writing review and editing. Evangelos Farantatos: project administration, supervision, writing review and editing. Ilhan Kocar: conceptualization, investigation, project administration, resources, supervision, writing, review & editing. Siqi Bu: funding acquisition, project administration, and resources. All authors read and approved the final manuscript.

FUNDING

This work is supported by the Hong Kong Research Grant Council for the Research Project (No. 15229421) and the PolyU Presidential PhD Fellowship Scheme.

AVAILABILITY OF DATA AND MATERIALS

Please contact the corresponding author for data material request.

DECLARATIONS

Competing interests: The authors declare that they have no known competing financial interests or personal relationships that could have appeared to influence the work reported in this article.

AUTHORS' INFORMATION

Xinquan Chen received the B.S. and M.S. degrees in electrical engineering from the South China University of Technology, Guangzhou, China, in 2018 and 2021, respectively. He is currently pursuing a Ph. D. degree in Department of Electrical and Electronic Engineering at The Hong Kong Polytechnic University. His research interests include power system dynamics and protection, inverter control, renewable energy sources, and HVDC technology.

Aboutaleb Haddadi received the Ph.D. degree in electrical and computer engineering from McGill University, Montréal, QC, Canada, in 2015. From 2015 to 2020, he was a postdoctoral fellow and research associate with Polytechnique Montréal, Montréal, QC, Canada. Since 2020, he has been with the Electric Power Research Institute, Palo Alto, CA, USA, as a senior engineer/scientist and technical lead/project manager, where he leads R&D activities related to bulk system and distributed renewable energy resources modeling and system integration impacts. Dr. Haddadi is also the EPRI Manager of the Advanced Grid Innovation Lab for Energy of the New York Power Authority, White Plains, NY, USA. He is the Chair of CIGRE working group C4.60 and is further active in a number of working groups of IEEE Power and Energy Society, Western Electricity Coordinating Council, and North American Electric Reliability Corporation. His research interests include renewable resource integration, power system protection, power system modeling and simulation.

Evangelos Farantatos received the Diploma in electrical and computer engineering from the National Technical University of Athens, Athens, Greece, in 2006, and the M.S. and Ph.D. degrees from the Georgia Institute of Technology, Atlanta, GA, USA, in 2009 and 2012, respectively. He is currently a Principal Project Manager with Grid Operations and Planning R&D Group, EPRI, Palo Alto, CA, USA. He is managing and leading the technical work of various R&D projects related to synchrophasor technology, power systems monitoring and control, power systems stability and dynamics, renewable energy resources modeling, grid operation with high levels of inverter-based resources and system protection. In summer 2009, he was an Intern with MISO.

Ilhan Kocar received the B.Sc. and M.Sc. degrees in EEE from Orta Doğu Teknik Üniversitesi, Ankara, Türkiye, in 1998 and 2003, respectively, and the Ph.D. degree in EE from École Polytechnique de Montréal (affiliated with Université de Montréal), QC, Canada, in 2009. He has 25 years of diverse experience in the power engineering field across industry, academia, and major regions including North America, Asia, and Europe. He is a full professor at Polytechnique Montréal and CEO of DIgSILENT North America Inc. His research aims to address critical challenges in integrating renewable energy sources into power systems. He serves as an Editor of *IEEE Transactions on Power Delivery*.

Siqi Bu received the Ph.D. degree from the electric power and energy research cluster, The Queen's University of Belfast, Belfast, U.K., where he continued his postdoctoral research work before entering industry. Then he was with National Grid UK as an experienced UK National Transmission System Planner and Operator. He is an associate professor and associate head with Department of Electrical and Electronic Engineering, The Hong Kong Polytechnic University, Kowloon, Hong Kong, and associate director of Research Centre for Grid Modernization. He is also a chartered engineer with UK Royal Engineering Council, London, U.K. and a Fellow of IET. His research interests include power system stability, operation and economics considering renewable energy integration, smart grid application and transport electrification. Dr Bu is an Editor of *IEEE Transactions on Power Systems*, *IEEE Transactions on Consumer Electronics*, *IEEE Power Engineering Letters*, *IEEE Access*, *IEEE Open Access Journal of Power and Energy*, *CSEE Journal of Power and Energy Systems*, *Protection and Control of Modern Power Systems*, *Journal of Modern Power Systems and Clean Energy* and *Advances in Applied Energy*.

REFERENCES

[1] Erdiwansyah, Mahidin, and H. Husin *et al.*, "A critical review of the integration of renewable energy sources with various technologies," *Protection and Control of Modern Power Systems*, vol. 6, no. 1, pp. 1-18, Jan. 2021.

[2] M. Zhang, Y. Han, and Y. Liu *et al.*, "Multi-timescale modeling and dynamic stability analysis for sustainable microgrids: state-of-the-art and perspectives," *Protection and Control of Modern Power Systems*, vol. 9, no. 3, pp. 1-35, May 2024.

[3] P. Sun, Z. Tian, and M. Huang *et al.*, "Additional kinetic energy injection and piecewise damping based postfault anti-windup and transient stability enhanced control for grid-forming inverter," *IEEE Transactions on Power Electronics*, vol. 39, no. 7, pp. 8007-8023, Jul. 2024.

[4] U. Markovic, O. Stanojev, and P. Aristidou *et al.*, "Understanding small-signal stability of low-inertia systems," *IEEE Transactions on Power Systems*, vol. 36, no. 5, pp. 3997-4017, Sept. 2021.

[5] P. Singh, U. Kumar, and N. K. Choudhary *et al.*, "Advancements in protection coordination of microgrids: a comprehensive review of protection challenges and mitigation schemes for grid stability," *Protection and Control of Modern Power Systems*, vol. 9, no. 6, pp. 156-183, Nov. 2024.

[6] A. N. Sheta, G. M. Abdulsalam, and B. E. Sedhom *et al.*, "Comparative framework for AC-microgrid protection schemes: challenges, solutions, real applications, and future trends," *Protection and Control of Modern Power Systems*, vol. 8, no. 2, pp. 1-40, Apr. 2023.

[7] H. Zhang, W. Xiang, and W. Lin *et al.*, "Grid forming converters in renewable energy sources dominated power grid: control strategy, stability, application, and challenges," *Journal of Modern Power Systems and Clean Energy*, vol. 9, no. 6, pp. 1239-1256, Nov. 2021.

[8] A. Tayyebi, D. Gross, and A. Anta *et al.*, "Frequency stability of synchronous machines and grid-forming power converters," *IEEE Journal of Emerging and Selected Topics in Power Electronics*, vol. 8, no. 2, pp. 1004-1018, Jun. 2020.

[9] Q. Hu, R. Han, and X. Quan *et al.*, "Grid-forming inverter enabled virtual power plants with inertia support capability," *IEEE Transactions on Smart Grid*, vol. 13, no. 5, pp. 4134-4143, Sept. 2022.

[10] J. Wang and K. Ma, "Inertia and grid impedance emulation of power grid for stability test of grid-forming converter," *IEEE Trans actions on Power Electronics*, vol. 38, no. 2, pp. 2469-2480, Feb. 2023.

[11] M. Ferrari, L. M. Tolbert, and E. C. Piesciorovsky, "Grid forming inverter with increased short-circuit contribution to address inverter-based microgrid

protection challenges," *IEEE Open Journal of the Industrial Electronics Society*, vol. 5, pp. 481-500, Jun. 2024.

[12] N. Fischer, G. Benmouyal, and D. Hou *et al.*, "Tutorial on power swing blocking and out-of-step tripping," in *Proceedings of 39th Annual Western Protective Relay Conference*, Washington, USA, Nov. 2012, pp. 1-22.

[13] S. Bahari, H. Seyedi, and K. Zare, "Improving power swing detection in the presence of doubly-fed induction generator wind farms based on setting adaptation," *Electric Power Systems Research*, vol. 224, Nov. 2023.

[14] S. A. Hosseini, B. Taheri, and H. A. Abyaneh *et al.*, "Comprehensive power swing detection by current signal modeling and prediction using the GMDH method," *Protection and Control of Modern Power Systems*, vol. 6, no. 2, pp. 1-11, Apr. 2021.

[15] S. M. Hashemi, M. Sanaye-Pasand, and M. Shahidehpour, "Fault detection during power swings using the properties of fundamental frequency phasors," *IEEE Transactions on Smart Grid*, vol. 10, no. 2, pp. 1385-1394, Mar. 2019.

[16] M. K. Gunasegaran, C. Tan, and A. H. A. Bakar *et al.*, "Progress on power swing blocking schemes and the impact of renewable energy on power swing characteristics: a review," *Renewable and Sustainable Energy Reviews*, vol. 52, pp. 280-288, Jan. 2015.

[17] Y. Xiong, H. Wu, and X. Wang, "Efficacy analysis of power swing blocking and out-of-step tripping protection for grid-following-VSC systems," in *the 2023 8th IEEE Workshop on the Electronic Grid (eGRID)*, Karlsruhe, Germany, Nov. 2023.

[18] A. Haddadi, I. Kocar, and U. Karaagac *et al.*, "Impact of wind generation on power swing protection," *IEEE Transactions on Power Delivery*, vol. 34, no. 3, pp. 1118-1128, Jun. 2019.

[19] C. Fang, L. Mu, and Z. Wang *et al.*, "Analysis of grid-forming IIDG's transient- and steady-state fault model," *IEEE Transactions on Smart Grid*, vol. 13, no. 2, pp. 1187-1199, Mar. 2022.

[20] Y. Li, Y. Lu, and J. Yang *et al.*, "Transient stability of power synchronization loop based grid forming converter," *IEEE Transactions on Energy Conversion*, vol. 38, no. 4, pp. 2843-2859, Dec. 2023.

[21] F. M. Gonzalez-Longatt, J. L. Rueda, and P. Palensky *et al.*, "Investigations of the virtual impedance control mode of synchronverter in the power swing," in *the 2022 International Conference on Smart Energy Systems and Technologies (SEST)*, Eindhoven, Netherlands, Sept. 2022.

[22] M.-A. Nasr and A. Hooshyar, "Power swing in systems with inverter-based resources—part I: dynamic model development," *IEEE Transactions on Power Delivery*, vol. 39, no. 3, pp. 1889-1902, Jun. 2024.

[23] M.-A. Nasr and A. Hooshyar, "Power swing in systems with inverter-based resources—part II: impact on protection systems," *IEEE Transactions on Power Delivery*, vol. 39, no. 3, pp. 1903-1917, Jun. 2024.

[24] Y. Xiong, H. Wu, and X. Wang, "Efficacy analysis of legacy dual-blinder-based power swing detection scheme in grid-forming VSC-based power system," in *the 22nd Wind and Solar Integration Workshop (WIW 2023)*, Copenhagen, Denmark, Nov. 2023.

[25] Y. Gu and T. C. Green, "Power system stability with a high penetration of inverter-based resources," *Proceedings of the IEEE*, vol. 111, no. 7, pp. 832-853, Jul. 2023

[26] D. Pan, X. Wang, and F. Liu *et al.*, "Transient stability of voltage-source converters with grid-forming control: a design-oriented study," *IEEE Journal of Emerging and Selected Topics in Power Electronics*, vol. 8, no. 2, pp. 1019-1033, Jun. 2020.

[27] X. Xiong, C. Wu, and B. Hu *et al.*, "Transient damping method for improving the synchronization stability of virtual synchronous generators," *IEEE Transactions on Power Electronics*, vol. 36, no. 7, pp. 7820-7831, Jul. 2021.

[28] K.H. Kim, Y. C. Jeung, and D. C. Lee *et al.*, "LVRT scheme of PMSG wind power systems based on feedback linearization," *IEEE Transactions on Power Electronics*, vol. 27, no. 5, pp. 2376-2384, May 2012.

[29] J. Machowski, J. W. Bialek, and J. Bumby, "*Power System Dynamics: Stability and Control*," Wiley, 2011.

[30] M. Alizadeh, X. Wang, and L. Chen *et al.*, "Sustained oscillations in modern AC distribution systems with high DER infiltration," *IEEE Transactions on Power Systems*, vol. 40, no. 1, pp. 244-255, Jan. 2024.

[31] Z. Hong, H. Xu, and Z. Hou *et al.*, "Origin of anomalous instability of grid-forming converters tied to stiff grid," *IET Renewable Power Generation*, vol. 17, no. 10, pp. 2563-2574, Jun. 2023.

[32] X. Chen, C. Wu, and Y. Wang, "An improved virtual impedance method for single-loop controlled grid-forming inverters to suppress low-frequency oscillations," in *the 2024 IEEE 10 th International Power Electronics and Motion Control Conference (IPEMC2024-ECCE Asia)*, Chengdu, China, May 2024.

[33] A. D. Paquette and D. M. Divan, "Virtual impedance current limiting for inverters in microgrids with synchronous generators," *IEEE Transactions on Industrial Application*, vol. 51, no. 2, pp. 1630-1638, Mar. 2015.